


# Mott resistive switching initiated by topological defects

Received: 16 April 2024

Accepted: 15 October 2024

Published online: 31 October 2024

 Check for updates

Alessandra Milloch <sup>1,2,3</sup> , Ignacio Figueruelo-Campanero <sup>4,5</sup> , Wei-Fan Hsu <sup>2</sup>, Selene Mor <sup>1,3</sup>, Simon Mellaerts <sup>2</sup>, Francesco Maccherozzi <sup>6</sup>, Larissa S. I. Veiga<sup>6</sup>, Sarnjeet S. Dhesi <sup>6</sup>, Mauro Spera <sup>1</sup>, Jin Won Seo <sup>7</sup>, Jean-Pierre Locquet <sup>2</sup>, Michele Fabrizio <sup>8</sup>, Mariela Menghini <sup>4</sup> & Claudio Giannetti <sup>1,3,9</sup> 

Avalanche resistive switching is the fundamental process that triggers the sudden change of the electrical properties in solid-state devices under the action of intense electric fields. Despite its relevance for information processing, ultrafast electronics, neuromorphic devices, resistive memories and brain-inspired computation, the nature of the local stochastic fluctuations that drive the formation of metallic regions within the insulating state has remained hidden. Here, using operando X-ray nano-imaging, we have captured the origin of resistive switching in a  $V_2O_3$ -based device under working conditions.  $V_2O_3$  is a paradigmatic Mott material, which undergoes a first-order metal-to-insulator phase transition together with a lattice transformation that breaks the three-fold rotational symmetry of the rhombohedral metallic phase. We reveal a new class of volatile electronic switching triggered by nanoscale topological defects appearing in the shear-strain based order parameter that describes the insulating phase. Our results pave the way to the use of strain engineering approaches to manipulate such topological defects and achieve the full dynamical control of the electronic Mott switching. Topology-driven, reversible electronic transitions are relevant across a broad range of quantum materials, comprising transition metal oxides, chalcogenides and kagome metals.

The insulator-to-metal transition (IMT) in Mott materials is a key mechanism for the development of next generation Motronic devices<sup>1,2</sup>. The intrinsic correlated nature of the Mott insulating state makes these systems fragile to external stimuli<sup>3,4</sup>, such as the application of an electric field, which can drive the collapse of the electronic band structure and the sudden release of a large number of free carriers<sup>5,6</sup>. At the macroscopic level, this phenomenon

manifests in the resistive switching process, i.e., a sharp increase of the current flow when the applied voltage exceeds a threshold value<sup>7–16</sup>. This strong non-linearity triggered many efforts to develop neuromorphic building blocks for the hardware implementation of neural networks<sup>17–24</sup> or for ultrafast volatile and non-volatile memories or processors<sup>25–27</sup>. The state-of-the-art macroscopic models<sup>28</sup> are based on resistor networks that consider

<sup>1</sup>Department of Mathematics and Physics, Università Cattolica del Sacro Cuore, Brescia, Italy. <sup>2</sup>Department of Physics and Astronomy, KU Leuven, Leuven, Belgium. <sup>3</sup>ILAMP (Interdisciplinary Laboratories for Advanced Materials Physics), Università Cattolica del Sacro Cuore, Brescia, Italy. <sup>4</sup>IMDEA Nanociencia, Cantoblanco, Madrid, Spain. <sup>5</sup>Facultad Ciencias Físicas, Universidad Complutense, Madrid, Spain. <sup>6</sup>Diamond Light Source, Didcot, Oxfordshire, UK. <sup>7</sup>Department of Materials Engineering, KU Leuven, Leuven, Belgium. <sup>8</sup>Scuola Internazionale Superiore di Studi Avanzati (SISSA), Via Bonomea 265, Trieste, Italy. <sup>9</sup>CNR-INO (National Institute of Optics), via Branzi 45, Brescia, Italy. ✉ e-mail: [alessandra.milloch@unicatt.it](mailto:alessandra.milloch@unicatt.it); [ignacio.figueruelo@imdea.org](mailto:ignacio.figueruelo@imdea.org); [claudio.giannetti@unicatt.it](mailto:claudio.giannetti@unicatt.it)

interconnected nodes transforming from the insulating to metallic state in the presence of an electric field. Above a certain threshold, a percolative, avalanche transition takes place, thus leading to the formation of conductive filaments and the consequent sudden drop in resistivity<sup>10,29</sup>.

The full control and exploitation of this process is currently prevented by a limited knowledge of the early-stage firing dynamics. Microscopically, little is known about the nature of the nanoscale regions that trigger the avalanche process. Also the relation between the electronic and structural properties of the switched regions and those of the pristine insulating template is a matter of debate. Pioneering optical microscopy experiments captured the real-time formation of macroscopic metallic channels<sup>30–34</sup>, but lacked the resolution and sensitivity to address the microscopic origin of the switching process.

Here, we adopt resonant X-ray microscopy to record nanoscale snapshots of the switching dynamics in a  $V_2O_3$ -based nanodevice during the application of an electric field. The results unveil the fundamental role played by the order parameter topology of the underlying lattice nanotexture. The breaking of the  $C_3$  symmetry upon transition to the insulating monoclinic phase leads to the formation of three twin shear-strain domains with boundaries oriented along the three hexagonal directions<sup>35,36</sup>. The geometrical constraints then produce shear-strain topological defects at the corners of monoclinic domains crossing with an angle of  $60^\circ$ . These nanoscale topological defects act as seeds for the formation of the metallic phase, thus triggering the macroscopic volatile resistive switching.

$V_2O_3$  is a prototypical Mott insulator that undergoes a thermally-driven transition from a high-temperature paramagnetic, rhombohedral metal to a low-temperature antiferromagnetic monoclinic insulator<sup>37–39</sup>. The lattice transformation at the critical temperature  $T_{IMT}$  implies the breaking of the  $C_3$  symmetry of the non-primitive hexagonal unit cell of the high-temperature metallic phase (see Fig. 1a). The structural transition can thus be described<sup>36</sup> by a vector order

parameter:

$$\boldsymbol{\epsilon} = (\epsilon_{31}, \epsilon_{23}) = \epsilon (\cos \phi_n, \sin \phi_n) \quad (1)$$

associated to the shear strain components  $\epsilon_{31}$  and  $\epsilon_{23}$  that characterize the monoclinic distortion. Below  $T_{IMT}$ , the amplitude of the order parameter,  $\epsilon$ , becomes non-zero, while the phase can assume three different values:

$$\phi_n = (2n - 1) \frac{\pi}{3} \quad (2)$$

corresponding to the distortion along the three equivalent hexagonal axes of the rhombohedral phase, indicated in the following by the versors  $\hat{\epsilon}_n$ ,  $n=1,2,3$  (see Fig. 1b).

Resistive switching can be induced by applying an electric field across a patterned micro-gap at temperatures close to  $T_{IMT}$ <sup>30,32,40</sup>. The resistive switching device investigated here is formed by a 20 nm  $V_2O_3$  film coated with gold electrodes.  $V_2O_3$  is grown by oxygen-assisted Molecular Beam Epitaxy on a (0001)- $Al_2O_3$  substrate with a 40 nm  $Cr_2O_3$  buffer layer to reduce any interfacial residual strain<sup>41</sup>. The resulting  $V_2O_3$  film has the  $c$ -axis oriented parallel to the surface normal, with  $T_{IMT} = 145$  K (see Supplementary Fig. 1). Two gold electrodes allow the application of an electric bias across the gap of width  $w = 2 \mu\text{m}$  and length  $l = 30 \mu\text{m}$  (Fig. 1c). The gap region between the electrodes is imaged using PhotoEmission Electron Microscopy (PEEM), combined with X-ray Linear Dichroism (XLD) at the  $L_{2,3}$  vanadium edge (513–530 eV, see Supplementary Fig. 2)<sup>35,36,42</sup>. The XLD-PEEM images are obtained from the normalized difference between images recorded with the light electric field vector,  $\boldsymbol{E}$ , perpendicular and  $16^\circ$  to the surface normal at a photon energy 520.6 eV. Since the XLD signal depends on the angle between the in-plane component of  $\boldsymbol{E}$  and the position dependent order parameter,  $\boldsymbol{\epsilon}(\mathbf{r})$ <sup>36</sup> (see Fig. 1b and c), this technique provides a map - with  $\sim 30$  nm spatial resolution - of the

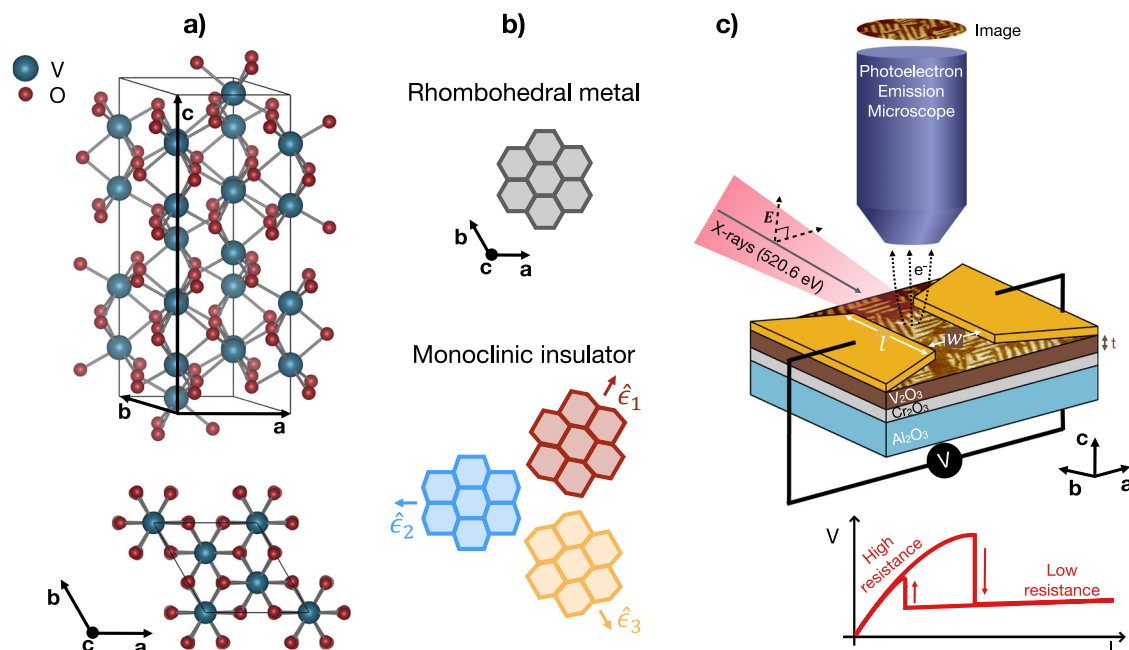


**Fig. 1 | Nanotexture of monoclinic  $V_2O_3$ .** **a** Non-primitive hexagonal unit cell of the  $V_2O_3$  high-temperature rhombohedral metallic phase. **b** Schematic of the rhombohedral-to-monoclinic distortion along each of the three equivalent hexagonal axes. **c** PEEM experimental setup. X-ray radiation, with tunable energy resonant with the vanadium  $L_{2,3}$  edge, impinges on the sample surface and the

emitted electrons are collected and imaged through electrostatic and magnetic lenses. The  $V_2O_3$  film is coated with gold metal electrodes, allowing to drive a current through the device (see sketch of a typical resistive switching current-voltage curve in the bottom panel) while simultaneously acquiring XLD-PEEM images.

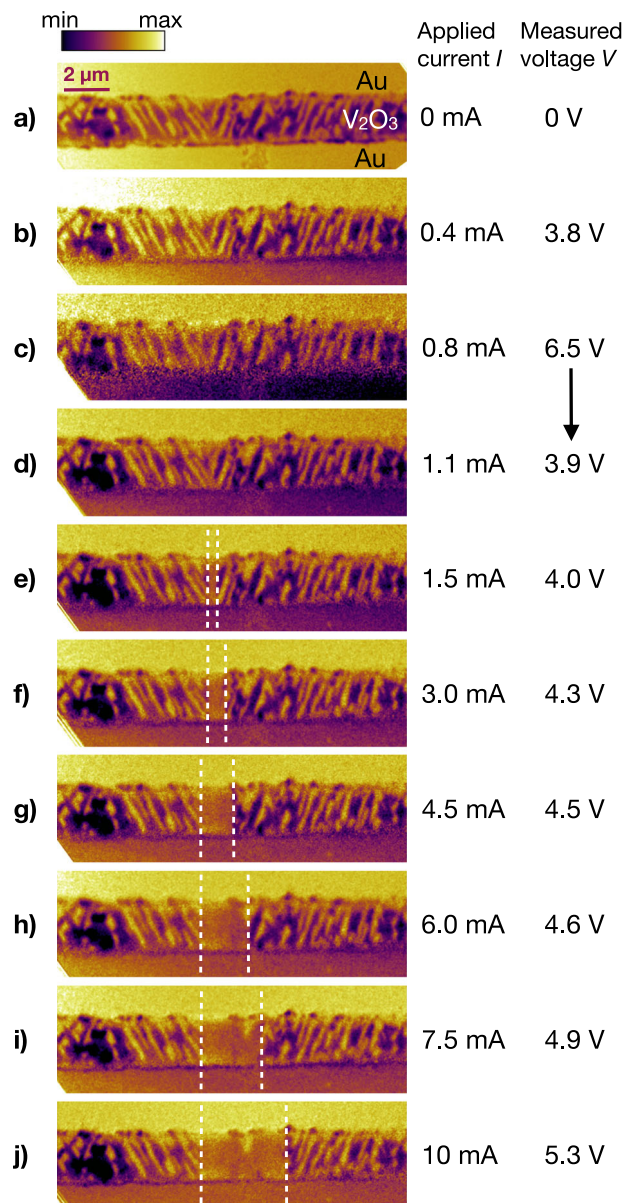


**Fig. 2 | PEEM imaging of resistive switching.** XLD-PEEM images before (a) and during (b–j) the application of an electric current at  $T = 120$  K. The homogeneous regions at the top and bottom of each image are the gold electrodes. The area in between is the exposed  $V_2O_3$  antiferromagnetic monoclinic phase, exhibiting a striped domain nanotexture. For currents larger than 1.5 mA, the striped domains disappear in the region delimited by the white dashed lines, demonstrating the appearance of a rhombohedral metallic filament, which widens as the current is increased.

three different monoclinic domains during the resistive switching process.

## Results and discussion

Figure 2a shows an XLD-PEEM image obtained in the monoclinic insulating phase at  $T = 120$  K. The  $V_2O_3$  nanotexture exhibits features typical of the monoclinic insulating phase<sup>35,36</sup>. Monoclinic domains with different  $\phi_n$  give rise to different XLD contrast, which can be identified as different color intensities within the XLD-PEEM image. The minimization of the total strain leads to the formation of stripe-like domains, with symmetry-constrained directions<sup>36</sup>. Each monoclinic insulating domain extends over a few micrometers, thus

connecting the two electrodes, and it is characterized by a width  $w_{dom} \sim 200$  nm<sup>36</sup>.

The XLD-PEEM imaging is then repeated while driving a current,  $I$ , through the device and measuring the voltage drop,  $V$ , across the gold contacts. Figures 2b–j show the XLD-PEEM images acquired at increasing values of  $I$ , following the upward branch of the hysteresis cycle. The presence of an in-plane electric field across the electrodes introduces a weak image blurring that becomes significant for  $V \geq 6$ –8 V. Despite this, the nanodomains are well resolved during the resistive switching process, which first manifests itself at the voltage drop observed between 0.8 mA and 1.1 mA (Fig. 2c and d, respectively). As the current is further increased, the melting of the monoclinic nanotexture in the region delimited by white dashed lines (Fig. 2e–j) progresses with a widening channel with a homogenous intensity. The XLD contrast measured in the region between the white dashed lines corresponds to the signal of the high-temperature rhombohedral phase. This is also confirmed from the angle dependence of the XLD signal<sup>36</sup>. As shown in Supplementary Fig. 3, images collected with two different X-rays polarization angles, with respect to the in-plane  $V_2O_3$  axes, show no intensity variation upon sample rotation in the metallic channel, as opposed to the lateral monoclinic domains, for which the XLD signal depends on the angle between the light polarization and  $\epsilon(\mathbf{r})$ . The constant XLD contrast region in the middle of the gap therefore appears due to the formation of a metallic channel with rhombohedral lattice structure ( $\epsilon=0$ ). XLD-PEEM images obtained under the same conditions, but with a larger field of view, capture the whole gap of the device (see Supplementary Fig. 4, which reports an independent set of PEEM measurements performed after thermal cycling to 250 K). The metallic channel consistently forms in the same location within the gap with no additional metallic paths observed. Furthermore, when the applied current is removed, the metallic channel disappears and the monoclinic domains reappear with the same pre-switching configuration, indicating a volatile process.

The formation of the metallic channel is pinned by a specific topology of the lattice nanotexture, characterized by V-shaped domains, i.e. at the crossing point of domains with the same  $\phi_n$  with directions that differ by  $\pi/3$ . Figure 3a shows a detail of the switching region, using a colorscale that highlights the three different domains with a monoclinic distortion along  $\hat{e}_1$  (red,  $\phi_1=\pi/3$ ),  $\hat{e}_2$  (blue,  $\phi_2=\pi$ ) and  $\hat{e}_3$  (yellow,  $\phi_3=5\pi/3$ ). The stabilization of the monoclinic nanotexture is driven by the Saint-Venant compatibility condition<sup>36</sup>, which ensures a continuity of the medium during a deformation via the curl-free condition:

$$\nabla \times \epsilon(\mathbf{r}) = 0. \quad (3)$$

The conservation of the parallel component of  $\epsilon(\mathbf{r})$  across an interface between two different domains has two important implications:

- the interface between two different monoclinic domains is oriented along  $\hat{e}_n$  of the third domain;
- the interface between a monoclinic and a rhombohedral metallic domain is oriented perpendicularly to  $\hat{e}_n$  of the monoclinic domain.

If we consider, for example, a domain with order parameter along  $\hat{e}_2$  (blue in Fig. 3b), its interface is oriented along  $\hat{e}_1$ , i.e. at  $\pi/3$  angle, when it neighbours an  $\hat{e}_3$  domain (yellow), whereas it is oriented along  $\hat{e}_3$ , i.e. at  $2\pi/3$  angle, when it neighbours an  $\hat{e}_1$  domain (red), in agreement with the nanotexture reported in Fig. 3. The Saint-Venant condition corresponds to a fixed phase jump  $\delta\phi=2\pi/3$  of  $\epsilon(\mathbf{r})$  across any interface between two monoclinic domains. We note that this condition is satisfied throughout the nanotextured domain structure, except at the V-shaped vertex structure formed by two  $\hat{e}_2$  domains with boundaries oriented along  $\hat{e}_1$  and  $\hat{e}_3$ . If we consider a circuit  $\Gamma_1$  across the boundary

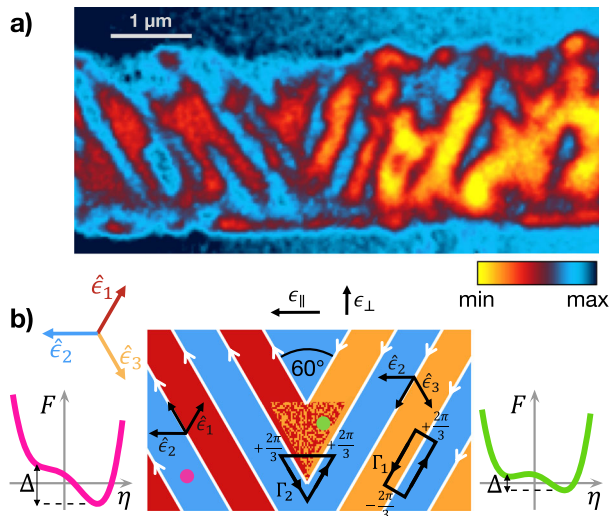


**Fig. 3 | Topological defect.** **a** Detail of the XLD-PEEM image shown in Fig. 2a in the region where the metallic filament is formed upon the application of a current above the threshold  $I_{th}$ . **b** Schematic of the monoclinic domains crossing at  $60^\circ$  and forming a topological defect. Blue, red and yellow areas identify the three possible monoclinic domains corresponding to the three equivalent order parameter directions  $\hat{\epsilon}_n$ . The order parameter at the boundaries between different domains is oriented along  $\hat{\epsilon}_1 + \hat{\epsilon}_2$  ( $2\pi/3$ ) for the red-blue interface and along  $\hat{\epsilon}_2 + \hat{\epsilon}_3$  ( $4\pi/3$ ) for the blue-yellow interface. The mixed red-yellow triangular region indicates the local suppression of the strain at the topological defect. The energy functionals shown on the left and right, illustrate how a topological defect (green plot, solid line) decreases the insulator-metal energy difference,  $\Delta$ .

between two striped domains, the total phase shift is given by  $\delta\phi = +2\pi/3 - 2\pi/3 = 0$  thus adhering to the curl-free condition in Eq. (3). In contrast, the topology of the V-shaped structure is such that, if we move around the internal apex ( $\Gamma_2$ ), the total phase-shift is constrained to  $\delta\phi = +2\pi/3 + 2\pi/3 = 4\pi/3$ , thus breaking the curl-free condition. The consequence is that the vertex of the V-shaped domains acts as a topological defect with a fractional Hopf index (see Supplementary Note 6). These topological defects are inherently characterized by the strong frustration of the local value of the order parameter  $\epsilon(\mathbf{r})$  and fluctuations on spatial and temporal scales that cannot be captured by the present experiment. We further note that the formation of the topological defect is a direct and unavoidable consequence of the quasi-1D confined geometry of the system. Whereas the component of the order parameter parallel to the electrodes ( $\epsilon_{\parallel}$ , see Fig. 3b) can be compensated outside the gap, the perpendicular component ( $\epsilon_{\perp}$ ) has to be minimized to avoid the accumulation of excessive strain energy within the gap region. Thus, considering the directions of  $\epsilon(\mathbf{r})$  at the boundaries between different monoclinic domains (see Fig. 3b), the formation of V-shaped domains is a unique configuration that fulfils the requirement  $\epsilon_{\perp} = 0$ .

The suppression of the symmetry-breaking order parameter,  $\epsilon(\mathbf{r})$ , at topological defects has far-reaching implications related to the nature of the resistive switching process. The electronic IMT can be described by a scalar order parameter  $\eta(\mathbf{r})$ <sup>36</sup>, which depends on the position  $\mathbf{r}$  and is such that  $\eta = -1$  in the metallic state and  $\eta = +1$  in the insulating state. The coupling between the electronic and structural transitions can be described by the energy functional<sup>36</sup>:

$$F[\epsilon, \eta] \propto \int d\mathbf{r} \left\{ (\eta^2(\mathbf{r}) - 1)^2 - g(\epsilon^2(\mathbf{r}) - \epsilon_t^2(V)) \eta(\mathbf{r}) \right\}, \quad (4)$$

where  $g$  is the coupling between the electronic order parameter and the strain and  $\epsilon_t(V)$  is a threshold parameter that controls the first-order IMT and can depend on the applied voltage  $V$ . When  $\epsilon^2(\mathbf{r}) > \epsilon_t^2(V)$ ,

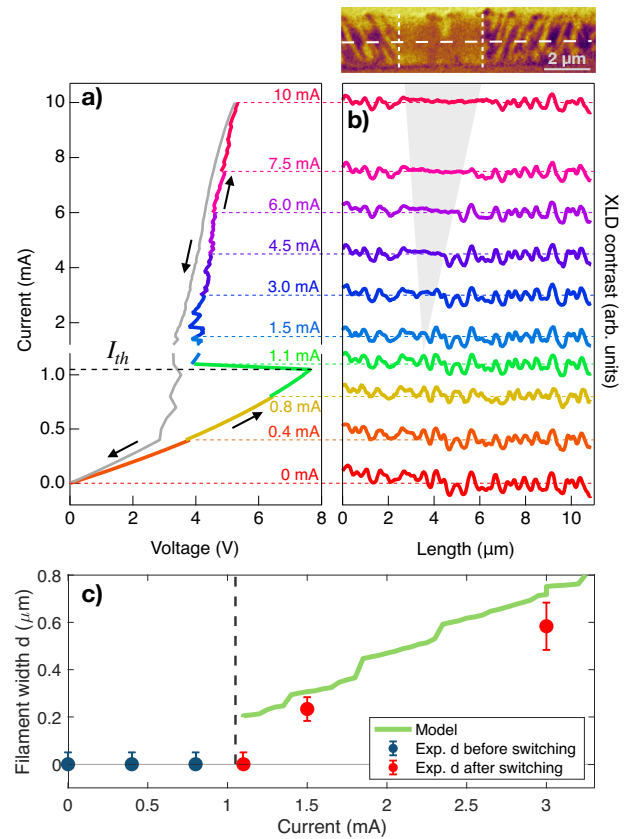


**Fig. 4 | Metallic channel formation.** **a**  $I$ - $V$  curve measured during the XLD-PEEM imaging. The sudden drop in the voltage measured at  $I_{th} = 1.05$  mA indicates the first resistive switch. **b** Line profiles of the XLD-PEEM images in Fig. 2. The grey shaded area indicates the progressive widening of the metallic rhombohedral filament. The direction of the line profiles is shown by the white dashed line in the XLD-PEEM image on top, where we report a detail of Fig. 2j. **c** Width,  $d$ , of the metallic filament as a function of current. The blue/red markers represent the values of  $d$  obtained from the XLD-PEEM images below/above  $I_{th}$ . The errorbars indicate the uncertainty in the filament width, estimated from the line profiles in panel b; when no filament is observed (first four data points,  $d = 0$ ), the errorbar is fixed to the experimental spatial resolution. The green solid line shows an estimate of  $d$ , derived from a parallel resistors model predicting a sudden jump of  $d$  to  $200 \mu\text{m}$  at  $I_{th}$  (see Supplementary Note 5).

the insulating phase with  $\eta = +1$  is locally favoured, whereas for strain smaller than the threshold value, i.e.  $\epsilon^2(\mathbf{r}) < \epsilon_t^2(V)$ , the metallic solution is stabilized.  $\epsilon_t^2(V)$  thus represents the threshold above which the insulating monoclinic state ( $\eta = +1, \epsilon \neq 0$ ) becomes stable. The description of the electric-field induced transition is based on the observation<sup>5</sup> that the electric field directly couples to the electronic bandstructure of a Mott insulator, making the metallic phase more stable. The transition can thus be described assuming that  $\epsilon_t^2(V)$  increases with increasing  $V$ . The energy difference between the insulating and metallic phase can be expressed as  $\Delta(\mathbf{r}, V) = F[-1] - F[+1] \simeq g[\epsilon^2(\mathbf{r}) - \epsilon_t^2(V)]$ . If we start from the insulating phase with  $\epsilon^2(\mathbf{r}) > \epsilon_t^2(V = 0)$ , the IMT takes place when  $V$  is increased up to the point that  $\Delta(\mathbf{r}, V) = 0$ . A topological defect, which locally suppresses  $\epsilon^2(\mathbf{r})$ , thus acts as a seed with a lower threshold compared to the rest of the system.

Intriguingly, we also note from Eq. (4) that the IMT can take place at a non-zero value of  $\epsilon^2(\mathbf{r})$ , which allows the formation of a non-thermal metallic state ( $\eta = -1$ ) with a finite monoclinic distortion ( $\epsilon^2(\mathbf{r}) \leq \epsilon_t^2(V)$ ), as already observed in non-equilibrium optical experiments<sup>36,43</sup>. The nature of the early-stage switching process can be inferred by a direct comparison between the electrical state of the

device and the melting of the monoclinic domains. The  $I-V$  curve of the device, as measured in-situ during the PEEM imaging, is plotted in Fig. 4a. XLD-PEEM images were recorded at specific values of  $I$ . The  $I-V$  plot shows that the first resistive switching event occurs at the threshold current  $I_{th} = 1.05$  mA. In Fig. 4b, we report a linecut of the XLD-PEEM image acquired at specific values of  $I$ ; the image profile is taken along a line crossing the monoclinic domains in the middle of the device gap (see white solid line in Fig. 4, top panel). For large currents running through the device, the line profile in Fig. 4b displays a flat region, which indicates the melting of the monoclinic nanodomains due to the formation of the rhombohedral metallic channel. As highlighted by the grey area in Fig. 4b, the width  $d$  of the metallic filament increases with the current, from  $d = 0.23 \pm 0.05 \mu\text{m}$  at  $I = 1.5$  mA to  $d = 3.7 \pm 0.2 \mu\text{m}$  at  $I = 10$  mA.

Modelling the device as a circuit with two parallel resistors (see Supplementary Note 5) allows an estimation of  $d$  of the rhombohedral filament corresponding to the observed voltage drop. For large currents running through the device, the experimentally determined values of  $d$  match well with those predicted for a metallic channel forming in the gap, which has the resistivity of the high-temperature rhombohedral phase, as shown in Fig. 4c, and in Supplementary Fig. 5a for the full current range. However, in correspondence of the first resistive switching event at  $I_{th} = 1.05$  mA, the model predicts the sudden formation of a  $\sim 200$  nm wide metallic rhombohedral filament, which is not visible in the XLD-PEEM images (see Fig. 4c and Supplementary Fig. 5), despite being well above the experimental resolution of the microscope. This is evidenced by PEEM imaging at  $I = 1.1$  mA, where no variation in the domain nanotexture is appreciated, while the simultaneous voltage measurement guarantees that the device has already switched. To explain this discrepancy, one might suspect that a rhombohedral metallic filament forms below the surface of the  $\text{V}_2\text{O}_3$  film, where it is not detected by PEEM which has a surface sensitivity limited to the first few nanometers. In fact, two arguments act against this possibility. i) The presence of the  $\text{Cr}_2\text{O}_3$  buffer layer reduces the substrate-film lattice mismatch from 4.2% to 0.1%, thus almost entirely removing the residual epitaxial strain in the film<sup>41</sup>, which is known to suppress the monoclinic phase and favour interfacial metallicity<sup>41,44</sup>. In contrast to highly-strained films, in which the metal to insulator resistivity jump is strongly suppressed<sup>44</sup>, the films in the present study display the 5-order of magnitude resistivity change typical of the unstrained metal-to-insulator transition (see Supplementary Fig. 1). ii) The curl-free conditions force the interface between monoclinic and rhombohedral metallic regions to be oriented perpendicularly to the order parameter of the monoclinic domain. The formation of a sub-surface metallic layer would lead to a sharp ( $\ll 20$  nm) monoclinic-rhombohedral interface parallel to  $\epsilon$ , thus leading to a dramatic increase of the strain energy of the system. Our results are compatible with a complex scenario in which the topology-driven resistive switching likely occurs via the sudden transformation of a single 200 nm wide insulating monoclinic area into a metallic channel with a non-thermal monoclinic lattice structure. At a second stage, the Joule heating leads to a local temperature increase and, consequently, to the thermally driven monoclinic-to-rhombohedral structural transition and the formation of a rhombohedral metallic channel perpendicular to both the metallic electrodes and the  $\hat{e}_2$  order parameter direction, as observed in Fig. 2.

The X-ray-based nanoimaging of a Mott device under operating conditions allowed us to simultaneously capture the formation of nanoscale conductive paths and the topology of the underlying symmetry-broken nanotexture. The present results expand our knowledge of the resistive switching process in Mott materials by demonstrating the leading role of inherent topological defects in initiating the avalanche process. The methodologies used in this work imply that nanoscale strain engineering approaches could unlock a gate to manipulating topological defects and controlling the

electronic switching dynamics in real devices, such as Mott-transition-based RRAM<sup>45,46</sup>, Mott memristor<sup>47-49</sup> and artificial neurons<sup>50,51</sup>. Fine tuning of crystal growth by adjustment of the substrate parameters<sup>52,53</sup>, manipulation of the geometry and orientation of metallic over-layers and use of nano-patterning approaches<sup>54</sup> represent possible viable routes to introduce topological defects in a controlled way via strain manipulation. The concept of topology-driven resistive switching will be key to assessing the possible non-thermal nature of the early stage electronic phase<sup>36</sup> as well as the microscopic origin of memory and non-volatile effects recently observed in Mott devices<sup>11</sup>. We note that the relation between topological defects and electronic phase transitions established here is a general concept, potentially extendable to other systems that undergo first-order phase transitions accompanied by a symmetry breaking, as described by the energy functional (4). Relevant examples embrace transition-metal oxides<sup>1,55</sup>, such as vanadates, nickelates and manganites, and layered materials, such as 1T-TaS<sub>2</sub><sup>56-59</sup>, in which the IMT is accompanied by charge-, lattice- and orbital-ordered states with reduced symmetry. Further platforms include cuprate superconductors<sup>60</sup> and kagome metals<sup>61</sup> in which light- or magnetic-induced discontinuous electronic transitions coexist with charge-order. Topological defects in the order parameter therefore provide a framework for understanding non-equilibrium electronic phase transitions, allowing all-optical control of hidden states of matter in a broad class of quantum materials<sup>59,62-66</sup>.

## Methods

### Samples

The  $\text{V}_2\text{O}_3$  sample is grown by oxygen-assisted molecular beam epitaxy (MBE) in a vacuum chamber with a base pressure of  $10^{-9}$  Torr and a growth temperature of 700°C. In order to relax the tensile strain in the  $\text{V}_2\text{O}_3$  film, a  $\text{Cr}_2\text{O}_3$  buffer layer is first grown on a (0001)- $\text{Al}_2\text{O}_3$  substrate, used without prior cleaning. V is evaporated from an electron gun with a flux of 0.1 Å/s, and an oxygen partial pressure of  $6.2 \times 10^{-6}$  Torr is used during the growth<sup>41</sup>. Under these conditions, a single crystalline epitaxial film with the  $c$ -axis oriented perpendicular to the surface is obtained. Temperature-dependent resistivity measurements (Supplementary Fig. 1) are performed in the Van der Pauw configuration using an Oxford Optistat CF2-V cryostat with a sweep rate of 1.0 K per minute.

### Device fabrication

The  $\text{V}_2\text{O}_3$  thin film is patterned using standard optical lithography using AZ1505 resist. After developing the exposed areas, we deposit 5 nm of Ti + 60 nm of Au in an electron beam evaporator with a base pressure in the range of  $10^{-9}$  mbar. Finally, the sample is lifted off in acetone and cleaned with IPA and  $\text{N}_2$  gas.

### Experimental setup

PEEM measurements have been performed at the I06 beamline at the Diamond Light Source synchrotron. The X-rays beam is tuned to 520.6 eV photon energy; two different linear polarizations, perpendicular and at  $16^\circ$  to the sample surface normal, are employed to image the photoemitted electrons. XLD-PEEM images are obtained from the average of the difference between 30 PEEM images acquired with the two polarizations, normalized to their sum<sup>35,36</sup>. Resistive switching is performed by driving a current through the  $\text{V}_2\text{O}_3$  device by means of a Keithley 2461 SourceMeter, which sources current  $I$  and measures voltage  $V$  across two gold electrodes. The current is swiped to a specific value  $I^*$ , which is then maintained constant while XLD-PEEM images are acquired.

### Data availability

The data generated in this study are available at: <https://hdl.handle.net/10807/291116>.

## References

1. Tokura, Y., Kawasaki, M. & Nagaosa, N. Emergent functions of quantum materials. *Nat. Phys.* **13**, 1056–1068 (2017).
2. Yang, Z., Ko, C. & Ramanathan, S. Oxide electronics utilizing ultrafast metal-insulator transitions. *Annu. Rev. Mater. Res.* **41**, 337–367 (2011).
3. Zhang, J. & Averitt, R. D. Dynamics and control in complex transition metal oxides. *Annu. Rev. Mater. Res.* **44**, 19–43 (2014).
4. Basov, D., Averitt, R. & Hsieh, D. Towards properties on demand in quantum materials. *Nat. Mater.* **16**, 1077–1088 (2017).
5. Mazza, G., Amaricci, A., Capone, M. & Fabrizio, M. Field-driven mott gap collapse and resistive switch in correlated insulators. *Phys. Rev. Lett.* **117**, 176401 (2016).
6. Suen, C. T. et al. Electronic response of a Mott insulator at a current-induced insulator-to-metal transition. *Nat. Phys.* <https://doi.org/10.1038/s41567-024-02629-3> (2024).
7. Wang, Z. et al. Resistive switching materials for information processing. *Nat. Rev. Mater.* **5**, 173–195 (2020).
8. Wouters, D. J., Menzel, S., Rupp, J. A. J., Hennen, T. & Waser, R. On the universality of the I-V switching characteristics in non-volatile and volatile resistive switching oxides. *Faraday Discuss.* **213**, 183–196 (2019).
9. Kalcheim, Y. et al. Non-thermal resistive switching in Mott insulator nanowires. *Nat. Commun.* **11**, 2985 (2020).
10. Stoliar, P. et al. Universal electric-field-driven resistive transition in narrow-gap mott insulators. *Adv. Mater.* **25**, 3222–3226 (2013).
11. del Valle, J., Ramirez, J. G., Rozenberg, M. J. & Schuller, I. K. Sub-threshold firing in Mott nanodevices. *Nature* **569**, 388–392 (2019).
12. Guiot, V. et al. Avalanche breakdown in GaTa<sub>4</sub>Se<sub>8-x</sub>Te<sub>x</sub> narrow-gap Mott insulators. *Nat. Commun.* **4**, 1722 (2013).
13. Nakamura, F. et al. Electric-field-induced metal maintained by current of the Mott insulator Ca<sub>2</sub>RuO<sub>4</sub>. *Sci. Rep.* **3**, 2536 (2013).
14. Fursina, A., Sofin, R., Shvets, I. & Natelson, D. Origin of hysteresis in resistive switching in magnetite is Joule heating. *Phys. Rev. B* **79**, 245131 (2009).
15. Fursina, A., Sofin, R., Shvets, I. & Natelson, D. Statistical distribution of the electric field-driven switching of the Verwey state in Fe<sub>3</sub>O<sub>4</sub>. *N. J. Phys.* **14**, 013019 (2012).
16. Janod, E. et al. Resistive switching in Mott insulators and correlated systems. *Adv. Funct. Mater.* **25**, 6287–6305 (2015).
17. Zhou, Y. & Ramanathan, S. Mott memory and neuromorphic devices. *Proc. IEEE* **103**, 1289–1310 (2015).
18. Mehonic, A. & Kenyon, A. J. Brain-inspired computing needs a master plan. *Nature* **604**, 255–260 (2022).
19. Adda, C. et al. Mott insulators: A large class of materials for Leaky Integrate and Fire (LIF) artificial neuron. *J. Appl. Phys.* **124**, 152124 (2018).
20. Pérez-Tomás, A. Functional oxides for photoneuromorphic engineering: toward a solar brain. *Adv. Mater. Interfaces* **6**, 1900471 (2019).
21. del Valle, J., Salev, P., Kalcheim, Y. & Schuller, I. K. A caloritronics-based Mott neuristor. *Sci. Rep.* **10**, 4292 (2020).
22. Zhang, Z. et al. Neuromorphic learning with Mott insulator NiO. *Proc. Natl. Acad. Sci.* **118**, e2017239118 (2021).
23. Deng, X. et al. A flexible mott synaptic transistor for nociceptor simulation and neuromorphic computing. *Adv. Funct. Mater.* **31**, 2101099 (2021).
24. Deng, S. et al. Selective area doping for Mott neuromorphic electronics. *Sci. Adv.* **9**, eade4838 (2023).
25. Waser, R. & Aono, M. Nanoionics-based resistive switching memories. *Nat. Mater.* **6**, 833–840 (2007).
26. Ielmini, D. Resistive switching memories based on metal oxides: mechanisms, reliability and scaling. *Semiconduct. Sci. Technol.* **31**, 063002 (2016).
27. Ran, Y. et al. A review of Mott insulator in memristors: The materials, characteristics, applications for future computing systems and neuromorphic computing. *Nano Res.* **16**, 1165–1182 (2023).
28. Lee, J. S., Lee, S. & Noh, T. W. Resistive switching phenomena: A review of statistical physics approaches. *Appl. Phys. Rev.* **2**, 031303 (2015).
29. Stoliar, P. et al. A leaky-integrate-and-fire neuron analog realized with a mott insulator. *Adv. Funct. Mater.* **27**, 1604740 (2017).
30. del Valle, J., Ramirez, J. G., Rozenberg, M. J. & Schuller, I. K. Challenges in materials and devices for resistive-switching-based neuromorphic computing. *J. Appl. Phys.* **124**, 211101 (2018).
31. Lange, M. et al. Imaging of electrothermal filament formation in a Mott insulator. *Phys. Rev. Appl.* **16**, 054027 (2021).
32. del Valle, J. et al. Spatiotemporal characterization of the field-induced insulator-to-metal transition. *Science* **373**, 907–911 (2021).
33. Babich, D. et al. Lattice contraction induced by resistive switching in chromium-doped V<sub>2</sub>O<sub>3</sub>: a hallmark of Mott physics. *arXiv preprint arXiv:2105.05093* (2021).
34. Luibrand, T. et al. Characteristic length scales of the electrically induced insulator-to-metal transition. *Phys. Rev. Research* **5**, 013108 (2023).
35. Ronchi, A. et al. Early-stage dynamics of metallic droplets embedded in the nanotextured Mott insulating phase of V<sub>2</sub>O<sub>3</sub>. *Phys. Rev. B* **100**, 075111 (2019).
36. Ronchi, A. et al. Nanoscale self-organization and metastable non-thermal metallicity in Mott insulators. *Nat. Commun.* **13**, 3730 (2022).
37. McWhan, D., Rice, T. & Remeika, J. Mott transition in Cr-doped V<sub>2</sub>O<sub>3</sub>. *Phys. Rev. Lett.* **23**, 1384 (1969).
38. McWhan, D. & Remeika, J. Metal-insulator transition in (V<sub>1-x</sub>Cr<sub>x</sub>)<sub>2</sub>O<sub>3</sub>. *Phys. Rev. B* **2**, 3734 (1970).
39. McWhan, D., Menth, A., Remeika, J., Brinkman, W. & Rice, T. Metal-insulator transitions in pure and doped V<sub>2</sub>O<sub>3</sub>. *Phys. Rev. B* **7**, 1920 (1973).
40. Guénon, S. et al. Electrical breakdown in a V<sub>2</sub>O<sub>3</sub> device at the insulator-to-metal transition. *Europhys. Lett.* **101**, 57003 (2013).
41. Dillemans, L. et al. Evidence of the metal-insulator transition in ultrathin unstrained V<sub>2</sub>O<sub>3</sub> thin films. *Appl. Phys. Lett.* **104**, 071902 (2014).
42. Park, J.-H. et al. Spin and orbital occupation and phase transitions in V<sub>2</sub>O<sub>3</sub>. *Phys. Rev. B* **61**, 11506 (2000).
43. Ronchi, A. et al. Light-assisted resistance collapse in a V<sub>2</sub>O<sub>3</sub>-based Mott-insulator device. *Phys. Rev. Appl.* **15**, 044023 (2021).
44. Pofelski, A. et al. Domain nucleation across the metal-insulator transition of self-strained V<sub>2</sub>O<sub>3</sub> films. *Phys. Rev. Materials* **8**, 035003 (2024).
45. Sawa, A. Resistive switching in transition metal oxides. *Mater. Today* **11**, 28–36 (2008).
46. Wang, Y. et al. Mott-transition-based RRAM. *Mater. Today* **28**, 63–80 (2019).
47. Pickett, M. D., Medeiros-Ribeiro, G. & Williams, R. S. A scalable neuristor built with Mott memristors. *Nat. Mater.* **12**, 114–117 (2013).
48. Yoshida, M., Suzuki, R., Zhang, Y., Nakano, M. & Iwasa, Y. Memristive phase switching in two-dimensional 1T-TaS<sub>2</sub> crystals. *Sci. Adv.* **1**, e1500606 (2015).
49. Kumar, S., Strachan, J. P. & Williams, R. S. Chaotic dynamics in nanoscale NbO<sub>2</sub> Mott memristors for analogue computing. *Nature* **548**, 318–321 (2017).
50. Tesler, F. et al. Relaxation of a spiking Mott artificial neuron. *Phys. Rev. Appl.* **10**, 054001 (2018).
51. Zhang, X. et al. An artificial spiking afferent nerve based on Mott memristors for neurobotics. *Nat. Commun.* **11**, 51 (2020).
52. Homm, P., Menghini, M., Seo, J. W., Peters, S. & Locquet, J. P. Room temperature Mott metal-insulator transition in V<sub>2</sub>O<sub>3</sub> compounds induced via strain-engineering. *APL Mater.* **9**, 021116 (2021).

53. Hsu, W.-F. et al. Raman spectroscopy and phonon dynamics in strained  $V_2O_3$ . *Phys. Rev. Mater.* **7**, 074606 (2023).
54. Meer, H. et al. Strain-induced shape anisotropy in antiferromagnetic structures. *Phys. Rev. B* **106**, 094430 (2022).
55. Imada, M., Fujimori, A. & Tokura, Y. Metal-insulator transitions. *Rev. Mod. Phys.* **70**, 1039–1263 (1998).
56. Vaskivskiy, I. et al. Controlling the metal-to-insulator relaxation of the metastable hidden quantum state in 1T-TaS<sub>2</sub>. *Sci. Adv.* **1**, e1500168 (2015).
57. Hollander, M. J. et al. Electrically driven reversible insulator-metal phase transition in 1T-TaS<sub>2</sub>. *Nano Lett.* **15**, 1861–1866 (2015).
58. Lee, S.-H., Goh, J. S. & Cho, D. Origin of the insulating phase and first-order metal-insulator transition in 1T-TaS<sub>2</sub>. *Phys. Rev. Lett.* **122**, 106404 (2019).
59. Gao, F. Y. et al. Snapshots of a light-induced metastable hidden phase driven by the collapse of charge order. *Sci. Adv.* **8**, eabp9076 (2022).
60. Keimer, B., Kivelson, S. A., Norman, M. R., Uchida, S. & Zaanen, J. From quantum matter to high-temperature superconductivity in copper oxides. *Nature* **518**, 179–186 (2015).
61. Asaba, T. et al. Evidence for an odd-parity nematic phase above the charge-density-wave transition in a kagome metal. *Nat. Phys.* **20**, 40–46 (2024).
62. Stojchevska, L. et al. Ultrafast switching to a stable hidden quantum state in an electronic crystal. *Science* **344**, 177–180 (2014).
63. Zhang, J. et al. Cooperative photoinduced metastable phase control in strained manganite films. *Nat. Mater.* **15**, 956–960 (2016).
64. Wandel, S. et al. Enhanced charge density wave coherence in a light-quenched, high-temperature superconductor. *Science* **376**, 860–864 (2022).
65. Cheng, Y. et al. Ultrafast formation of topological defects in a two-dimensional charge density wave. *Nat. Phys.* **20**, 54–60 (2024).
66. Verma, A. et al. Picosecond volume expansion drives a later-time insulator-metal transition in a nano-textured Mott insulator. *Nat. Phys.* **20**, 807–814 (2024).

## Acknowledgements

We thank Diamond Light Source for the provision of beamtime under proposal numbers MM27218, MM31711 and MM34455. We thank Manuel R. Osorio and Fernando J. Urbanos for the fabrication of sample electrodes at the Centre for Micro and Nanofabrication of IMDEA Nanociencia. C.G., A.M. and S.Mo. acknowledge financial support from MIUR through the PRIN 2017 (Prot. 20172H2SC4 005) and PRIN 2020 (Prot. 2020JLZ52N 003) programs and from the European Union - Next Generation EU, Missione 4 Componente 2, CUP J53D23001380008. Università Cattolica del Sacro Cuore contributed to the funding of this research project and its publication. S.Mo. acknowledges partial financial support through the grant “Finanziamenti ponte per bandi esterni” from Università Cattolica del Sacro Cuore. I.F.C. and M.M. acknowledge support from the “Severo Ochoa” Programme for Centres of Excellence in R&D (CEX2020-001039-S) and the Spanish AEI-MCIN PID2021-122980OB-C52 (ECOSOX-ECLIPSE). I.F.C. holds a FPI fellowship from the Spanish AEI-MCIN (PRE2020-092625). W.-F.H., S.Me., J.W.S. and J.-P.L. acknowledge financial support by the KU Leuven Research Funds Project No. C14/21/083, iBOF/21/084, KAC24/18/056 and C14/17/080, as well as the FWO AKUL/13/19 and AKUL/19/023, and the Research Funds

of the INTERREG-E-TEST Project (EMR113) and INTERREG-VL-VL-PATHFINDER Project (O559).

## Author contributions

A.M., I.F.C., W.-F.H., S.Mo., F.M., L.S.I.V., S.S.D., M.M., J.-P.L. and C.G. conceived the project and carried out the PEEM-resistive switching experiments at Diamond Light Source (UK). C.G. and M.M. coordinated the experimental activities with input from all the coauthors, in particular A.M. and I.F.C. A.M., I.F.C., W.-F.H., S.Mo., M.M., and C.G. analyzed the data. W.-F.H., S.Me., J.W.S. and J.-P.L. performed the MBE thin film growth, characterization and analysis. M.F. and M.S. developed the theoretical framework with main inputs from A.M. and C.G. A.M., M.F. and C.G. drafted the first version of the manuscript. All the authors participated in the discussion of the results and contributed to the revision of the manuscript.

## Competing interests

The authors declare no competing interests.

## Additional information

**Supplementary information** The online version contains supplementary material available at <https://doi.org/10.1038/s41467-024-53726-z>.

**Correspondence** and requests for materials should be addressed to Alessandra Milloch, Ignacio Figueruelo-Campanero or Claudio Giannetti.

**Peer review information** *Nature Communications* thanks Nicolas Gauquelin and the other, anonymous, reviewer(s) for their contribution to the peer review of this work. A peer review file is available.

**Reprints and permissions information** is available at <http://www.nature.com/reprints>

**Publisher's note** Springer Nature remains neutral with regard to jurisdictional claims in published maps and institutional affiliations.

**Open Access** This article is licensed under a Creative Commons Attribution-NonCommercial-NoDerivatives 4.0 International License, which permits any non-commercial use, sharing, distribution and reproduction in any medium or format, as long as you give appropriate credit to the original author(s) and the source, provide a link to the Creative Commons licence, and indicate if you modified the licensed material. You do not have permission under this licence to share adapted material derived from this article or parts of it. The images or other third party material in this article are included in the article's Creative Commons licence, unless indicated otherwise in a credit line to the material. If material is not included in the article's Creative Commons licence and your intended use is not permitted by statutory regulation or exceeds the permitted use, you will need to obtain permission directly from the copyright holder. To view a copy of this licence, visit <http://creativecommons.org/licenses/by-nc-nd/4.0/>.

© The Author(s) 2024